PHYSICAL REVIEW LETTERS

Amplitude and Phase of Tightly Focused Laser Beams in Turbid Media

Carole K. Hayakawa and Vasan Venugopalan*

*Department of Chemical Engineering and Materials Science, Engineering Tower, University of California,
Irvine, California 92697, USA*

Vishnu V. Krishnamachari and Eric O. Potma†

Department of Chemistry, Natural Sciences II, University of California, Irvine, California 92697, USA
(Received 13 January 2009; published 23 July 2009)

A framework is developed that combines electric field Monte Carlo simulations of random scattering with an angular-spectrum representation of diffraction theory to determine the amplitude and phase characteristics of tightly focused laser beams in turbid media. For planar sample geometries, the scattering-induced coherence loss of wave vectors at larger angles is shown to be the primary mechanism for broadening the focal volume. This approach for evaluating the formation of the focal volume in turbid media is of direct relevance to the imaging properties of nonlinear coherent microscopy, which rely on both the amplitude and phase of the focused fields.

Image quality in laser scanning optical microscopy is related directly to the spatial distribution and strength of the focal field. Diffraction theory models the focal volume as the spatial interference of the electric field and is sufficient to describe the propagation of a focused laser beam in homogeneous media [1]. However, biological samples are composed of cellular and extracellular components of varying size and refractive index [2,3] that act as scattering centers and distort the electric field [4]. Experiments show that focused beam propagation in turbid media results in attenuation of the focal field amplitudes and broadening of the focal spot along both lateral and axial dimensions [5]. Current formulations of diffraction theory, being limited to homogeneous media, cannot describe these important changes to the focal volume.

Monte Carlo methods can be used to solve the radiative transport equation by simulating light propagation as the transport of photons that undergo scattering at discrete locations within the turbid medium. Monte Carlo studies have shown the depth dependence and resolution of two- and three-photon excited fluorescence images to scale with the photon density in the focal region [5,6]. However, because particle-based Monte Carlo methods do not model the wave-characteristics of light, they are unable to model explicitly the amplitude and phase of tightly focused laser beams.

Complete knowledge of the focal field characteristics in turbid media is crucial for analysis of the resolution and signal strength in all forms of focused laser microscopy including fluorescence microscopy and optical coherence tomography. Moreover, the imaging properties of nonlinear coherent imaging methods, including multiharmonic generation and coherent anti-Stokes Raman scattering microscopy (CARS), in turbid samples cannot be understood without an evaluation of the amplitude and phase of focal fields [7]. Finite-difference time domain (FDTD) methods

can model explicitly the electric field propagation in turbid media [8,9]. However, FDTD calculations are computationally expensive and require the exact location and refractive index of the scattering centers within tissue; properties that are generally unknown. Consequently, modeling the general mechanisms that underlie the formation of the focal volume in turbid media remains a major challenge.

Here, we introduce a general framework that combines fully vectorial diffraction theory for focused fields with electric field Monte Carlo (EMC) simulations to determine the amplitude and phase of tightly focused fields in turbid media. The propagation of optical wave fronts is characterized by tracking the direction of the wave vector $\mathbf{k}$, its axial location (depth) within the medium, and the path length traveled between successive Mie scattering events using an EMC approach [10,11]. The connection with diffraction theory is made through the coherent angular dispersion function (CADF), which describes the amplitude loss and phase retardation associated with an optical wave front that enters a slab of specified thickness with direction $\mathbf{k}$ and exits the slab with direction $\mathbf{k}'$. The CADF is employed within an angular-spectrum representation of diffraction theory to calculate the full diffraction-limited focal field.

We decompose the incoming light into a set of plane waves, each characterized by x and y components of the wave-vector $\mathbf{k}$. Using an angular-spectrum representation, the electric field in the vicinity of the focal volume is

$$\mathbf{E}_f(x, y, z) = \frac{i f e^{-i k f}}{2\pi} \int_{(k_x^2 + k_y^2) \leq k^2} \mathbf{E}_{\text{far}}^d(k_x', k_y')$$
$$\times e^{i(k_x' x + k_y' y + k_z' z)} \frac{1}{k_z'} dk_x' dk_y', \qquad (1)$$

where f is the focal length of the lens and $\mathbf{E}_{\text{far}}^d$ is the

refracted field at the lens surface. The refracted field $\mathbf{E}_{\text{far}}^{d}$ is written in spherical coordinates as

$$\mathbf{E}_{\text{far}}^{d}(\theta', \phi') = \int_{\phi=0}^{2\pi} \int_{\theta=0}^{\pi/2} G(\theta, \phi|\theta', \phi') \mathbf{E}_{\text{far}}(\theta, \phi)$$
$$\times \sin\theta d\theta d\phi, \qquad (2)$$

$$\mathbf{E}_{\text{far}}(\theta, \phi) = \left(\frac{n_1}{n_2}\right)^{1/2} \sqrt{\cos\theta} \begin{pmatrix} \cos\phi\cos\theta\cos(\phi-\gamma) + \sin\phi\sin(\phi-\gamma) \\ \sin\phi\cos\theta\cos(\phi-\gamma) - \cos\phi\sin(\phi-\gamma) \\ \sin\theta\cos(\phi-\gamma) \end{pmatrix} |\mathbf{E}_{\text{inc}}(\theta, \phi)|, \qquad (3)$$

where γ is the angle of polarization of the incident field with respect to the x axis, and n_1 and n_2 are the refractive indices of the media before and after the refraction at the lens, respectively.

The CADF is determined by an EMC simulation. Similar to the situation encountered in the optical microscope, plane waves $\mathbf{k}$ are launched uniformly over a hemisphere $[0 \leq \phi < 2\pi, 0 \leq (\cos\theta) < 1]$ and propagate through a planar slab of thickness T [see Fig. 1(b)]. Each plane wave $\mathbf{k}$ is launched at given polar and azimuthal angles (θ, ϕ) and subject to scattering in the medium. The associated electric field is characterized by the coordinate system $(\hat{\mathbf{m}}, \hat{\mathbf{n}}, \hat{\mathbf{s}})$, where $\hat{\mathbf{s}}$ is the unit propagation direction of the photon and $\hat{\mathbf{m}}$ and $\hat{\mathbf{n}}$ are unit vectors in the direction of the parallel and perpendicular components of the polarized electric field: $\mathbf{E} = E_{\parallel}\hat{\mathbf{m}} + E_{\perp}\hat{\mathbf{n}}$.

Upon collision with a scatterer, whose probability per unit path length is characterized by the scattering coefficient μ_s of the medium, the wave's coordinate system is updated to $(\hat{\mathbf{m}}', \hat{\mathbf{n}}', \hat{\mathbf{s}}')$. The polar scattering angle Θ between the incoming and the outgoing wave is determined by sampling the angular distribution function $p(\Theta)$: [11]

$$p(\Theta) = \int_0^{2\pi} p(\Theta, \Phi)d\Phi = \frac{|S_1(\Theta)|^2 + |S_2(\Theta)|^2}{Q_{\text{sca}}x^2}, \qquad (4)$$
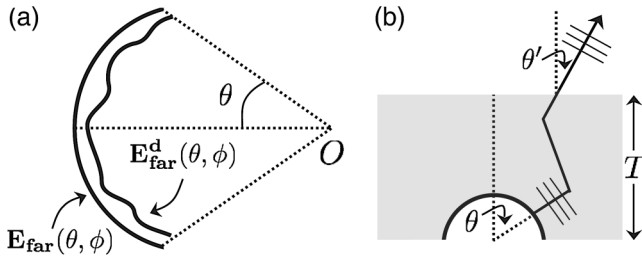

where $G(\theta, \phi|\theta', \phi')$ is the CADF per unit solid angle. For nonscattering media, $\mathbf{E}_{\text{far}}^{d} = \mathbf{E}_{\text{far}}$ and Eq. (1) is identical to the well-known diffraction integral [1,12]. $G(\theta, \phi|\theta', \phi')$ is used to modify the refracted field $\mathbf{E}_{\text{far}}$ to include the effects of scattering [see Fig. 1(a)]. For an aplanatic lens, the vector components of $\mathbf{E}_{\text{far}}(\theta, \phi)$ can be expressed in terms of the incident field, $\mathbf{E}_{\text{inc}}(\theta, \phi)$, as

where $p(\Theta, \Phi)$ is the scattering phase function, S_1 and S_2 are the angle-dependent elements of the amplitude scattering matrix, Q_{sca} is the scattering efficiency, and x is the particle size parameter [13]. The azimuthal scattering angle Φ is found using the rejection sampling method of the conditional probability $p(\Phi|\Theta) = p(\Theta, \Phi)/p(\Theta)$. The components of the normalized scattered field $\mathbf{E}'$ are calculated as

$$\begin{pmatrix} E_{\parallel}' \\ E_{\perp}' \end{pmatrix} = \frac{1}{\sqrt{N(\Theta, \Phi)}} \begin{pmatrix} S_2(\Theta)\cos\Phi & S_2(\Theta)\sin\Phi \\ -S_1(\Theta)\sin\Phi & S_1(\Theta)\cos\Phi \end{pmatrix} \begin{pmatrix} E_{\parallel} \\ E_{\perp} \end{pmatrix}, \qquad (5)$$

where $N(\Theta, \Phi)$ is the angle-dependent normalization factor [11]. Multiple scattering events introduce changes in both the propagation direction and polarization of the wave. Hence, after traversal through the slab, the propagation angles (θ', ϕ') of the outgoing wave front may differ from those of the incident wave front. The phase of the scattered fields is determined by the path length of the wave front as it passes through the slab and the phase shifts associated with the Mie scattering events. For a given polarization direction (ϕ'), the CADF is determined by the total coherent field $\langle E(\theta|\theta')\rangle/\sqrt{W(\theta')}$, obtained from the averaged sum of plane waves launched at θ and exiting at θ', where $W(\theta')$ is the total intensity exiting in the θ' direction. We also define an incoherent angular dispersion function (IADF) determined by $\langle |E(\theta|\theta')|\rangle/\sqrt{W(\theta')}$.

This approach fully characterizes electric field propagation in any medium in which the scattering events can be treated independently. Here, we wish to apply our framework to simulate the specific case of random scattering as it best captures the evolution of the focal field with depth in turbid media. In this case, the resulting electric field is determined for numerous realizations of particle arrangements resulting in a position-independent incoherent background in addition to the coherent fields that form the focal volume. While this methodology can be applied to a sample with fixed scatterers, the resulting predictions would reveal spatial interference patterns (speckle) and obscure the overall variation of the focal field characteristics.

We consider planar slabs of 10% intralipid solution, a highly turbid medium with scattering coefficient $\mu_s = 273.3 \text{ cm}^{-1}$ and absorption coefficient $\mu_a = 0.02 \text{ cm}^{-1}$

FIG. 1. (a) Schematic of the diffraction geometry. The wave front of the initial field $\mathbf{E}_{\text{far}}$ is modified to $\mathbf{E}_{\text{far}}^{\mathbf{d}}$, which captures the effects of a given medium. The diffraction pattern of the scattered field is determined in the vicinity of the focal spot O. (b) Schematic of the geometry used to calculate $G(\mathbf{k}|\mathbf{k}')$. Waves launched from a Lambertian source (symbolized by the semicircle) at angle θ are allowed to scatter in a medium of thickness T, and the amplitude and phase at each exit angle θ' is determined.

at $\lambda = 800$ nm. Spherical lipid particles of radius 0.1913 μm are chosen to match the experimentally determined first moment of the angular distribution function $g = 0.636$. These properties result in a scattering mean free path $l_s = 36.6$ μm and a transport mean free path $l^* = 100$ μm. We consider a water-immersion objective lens with numerical aperture 1.1 and linearly x-polarized light defined by $E_\parallel = 1$ and $E_\perp = 0$. Upon exiting the slab, we determine the component of the light polarized parallel to the incident wave front. For the EMC simulations, we launched 10^9 plane waves resulting in a relative error of $<3\%$ in the IADF.

In Fig. 2 two-dimensional representations of scattering-induced angular dispersion are shown for turbid planar slabs of thickness $T = 1$ μm and 150 μm. The graphs provide a measure of the probability by which optical wave fronts that enter the slab at a specific angle (θ) will exit the slab at another angle (θ'). The IADF is shown in Figs. 2(a) and 2(b). For the 1 μm slab, due to the limited number of scattering events, the IADF has diagonal elements of essentially constant magnitude, a result expected for nonscattering media. By contrast, propagation through the 150 μm thick slab involves multiple scattering events and results in a significant dispersion of the angular distribution of the optical wave fronts off the diagonal.

Two-dimensional representations of the CADF for the 1 μm and 150 μm slabs are shown in Figs. 2(c) and 2(d), respectively. For the 1 μm thick slab, the coherent fraction of the light is largely represented by the waves that have not undergone scattering, as evidenced by the diagonal in the graph. For propagation through the 150 μm slab, an almost similar trend is observed, indicating that the coherent amplitude predominantly stems from unscattered light.

Note that for both slabs, the off-diagonal elements of the CADF [Figs. 2(c) and 2(d)] are much smaller than their IADF counterparts [Figs. 2(a) and 2(b)]. This indicates that waves exiting at an angle θ' different than their entrance angle θ undergo different phase delays, and thus do not constructively interfere. Moreover, the coherent amplitude of the larger entrance angles θ is strongly attenuated. This is due to the longer path lengths that large θ-angle waves experience through the medium, which increases the likelihood of scattering, degrades coherence, and reduces the effective numerical aperture of the focused coherent radiation.

Figure 3 shows the calculated focal fields. After traversing the 1 μm thick slab, the focal field resembles the well-known amplitude of the Airy disk, as shown in Fig. 3(a). The phase profile of the focal field, shown in the inset, is nearly identical to the spatial phase associated with the Airy disk. Figure 3(b) shows the axial distribution of the focal field which resembles the focal volume known from standard diffraction theory. Thus for thin turbid samples the diffraction-limited focal volume is qualitatively unaffected.

The situation is very different for propagation across the 150 μm thick slab. First, as shown in Fig. 3(c), the central peak in the focal plane is broadened and the diffraction rings prominent at lower depths have virtually disappeared. Similar losses in spatial confinement along the axial direction are shown in Fig. 3(d) where the focus is much more extended and dispersed as compared to the focal field produced after traversal across a thin slab [Fig. 3(b)]. Surprisingly, while the first diffraction maximum has broadened, the phase profile still retains its sharp features, as seen in the inset of Fig. 3(c). The well-behaved phase profile is achieved because the actual diffraction-limited volume is the result of spatial interference of the in-phase components of the focal field. The dispersion of the focal volume at greater depths is due to the greater attenuation
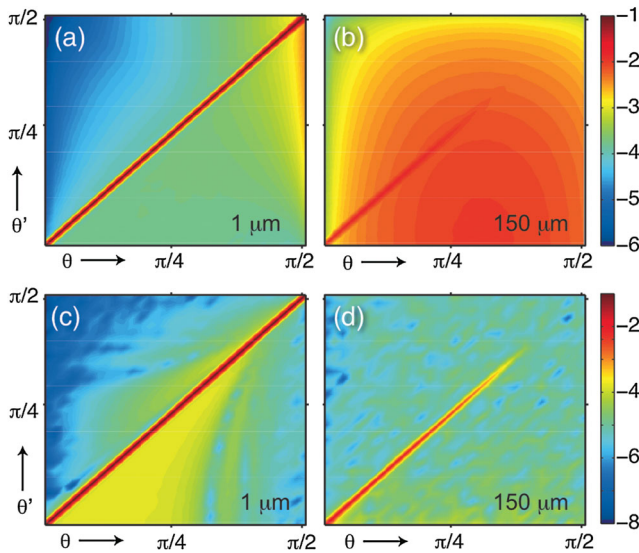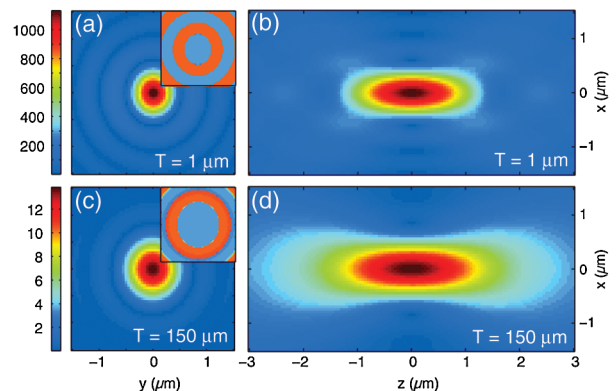

FIG. 2 (color). Incoherent and coherent angular dispersion in scattering media. IADF, for slab thicknesses of (a) $T = 1$ μm, and (b) $T = 150$ μm. CADF, for slab thicknesses of (c) $T = 1$ μm, and (d) $T = 150$ μm. Graphs are plotted on a logarithmic scale.

FIG. 3 (color). Focal field amplitude for a 1 μm thick slab (a), (b) and a 150 μm thick slab (c),(d). The amplitudes in the focal plane (xy) are given in (a) and (c), whereas (b) and (d) depict the xz cross sections. The insets show the phase pattern with values 0 (blue) and π (orange), and have the same dimensions as the amplitude plots.
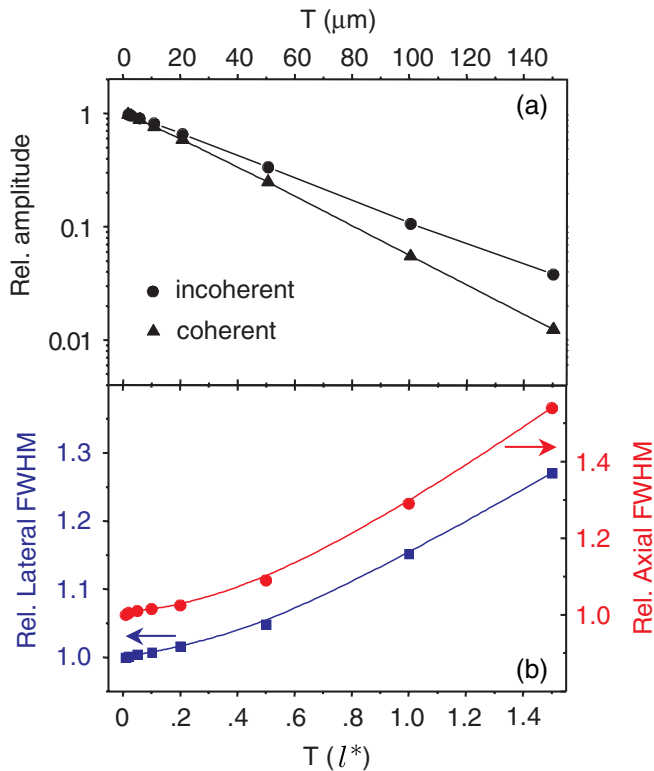
FIG. 4 (color online).   Depth dependence of the focal volume.
(a) Relative coherent and incoherent amplitude of the
x-polarized light. Incoherent amplitude is determined from the
transmission of the light propagating along $\theta = 0$. (b) Full width
at half maximum (FWHM) of the focal amplitude along lateral
(solid squares) and axial dimensions (solid circles). Medium
thickness is expressed in units of $l^* = 100 \ \mu m$.

experienced by the larger θ wave fronts in this planar slab
geometry.

Scattering in the medium reduces the portion of the field
that can interfere constructively in the focal volume.
Figure 4(a) plots the coherent amplitude of the focal field
as a function of slab thickness T. Both the depolarization of
the incident light and the loss of phase coherence between
the waves contribute to a rapid decline of the coherent
amplitude as a function of propagation depth in the scat-
tering medium. As expected, the depth-dependent coherent
amplitude exhibits a sharper exponential decay than the
incoherent amplitude. Along with the decrease of coherent
amplitude, the lateral and the axial dimensions of the focal
volume increase with slab thickness [Fig. 4(b)], and agrees
with the trend observed experimentally [5].

We have introduced a framework for the analysis of
focal fields produced in turbid media that combines electric
field Monte Carlo simulations of scattering with diffraction
theory. Our method is computationally inexpensive and
readily applicable to a large number of sample geometries.
Importantly, the framework provides a clear separation of
scattering (via the CADF) and diffraction, which enables
an intuitive interpretation of their contributions to the

formation of the focal field. Unlike FDTD methods, this
approach can predict the focal field distribution for *any*
incident beam profile without recomputing the effects
of scattering by the sample. Unlike particle-based
Monte Carlo simulations, in which diffraction can only
be modeled phenomenologically, the current framework
models the physics of the spatial dispersion of focal vol-
umes in turbid media. The depth-dependent CADF shows
that the observed broadening of the focal field is due
principally to the increased rate of coherence loss for field
components launched at larger angles θ; effectively reduc-
ing the numerical aperture of the wave front. The gradual
coherence loss for larger angles also smooths the diffrac-
tion pattern, manifest by diminished higher-order diffrac-
tion maxima at greater depths. Despite the quantitative loss
of coherence, the diffraction volume itself is governed by
the in-phase components of the field, which still yields a
flat phase front at the first maximum of the diffraction
pattern. This result is directly relevant to nonlinear coher-
ent microscopy techniques, which rely on the spatial co-
herence of the wave front in the vicinity of the focal
volume.

*vvenugop@uci.edu
†epotma@uci.edu

[1] B. Richards and E. Wolf, Proc. R. Soc. London, Sect. A:
Math. **253**, 358 (1959).
[2] J. M. Schmitt and G. Kumar, Opt. Lett. **21**, 1310 (1996).
[3] M. Hunter, V. Backman, and G. Popescu *et al.*, Phys. Rev.
Lett. **97**, 138102 (2006).
[4] V. Tuchin, *Tissue Optics* (SPIE Press, Bellingham, 2007).
[5] A. K. Dunn, V. P. Wallace, and M. Coleno *et al.*, Appl.
Opt. **39**, 1194 (2000).
[6] X. S. Gan and M. Gu, Opt. Lett. **24**, 741 (1999); X. Deng
and M. Gu, Appl. Opt. **42**, 3321 (2003).
[7] B. R. Masters and P. T. C. So, *Handbook of Biomedical
Nonlinear Optical Microscopy* (Oxford University Press,
New York, 2008).
[8] A. Dunn and R. Richards-Kortum, IEEE J. Sel. Top.
Quantum Electron. **2**, 898 (1996).
[9] C. Liu, C. Capjack, and W. Rozmus, J Biomed. Opt. **10**,
014007 (2005).
[10] V. R. Daria, C. Saloma, and S. Kawata, Appl. Opt. **39**,
5244 (2000).
[11] M. Xu, Opt. Express **12**, 6530 (2004).
[12] L. Novotny and B. Hecht, *Principles of Nano-Optics*
(Cambridge University Press, Cambridge, England, 2006).
[13] C. F. Bohren and D. R. Huffman, *Absorption and
Scattering of Light by Small Particles* (Wiley-VCH
Verlag GmbH, Mörlenbach, 1983).